

LA-UR-12-25613

Approved for public release; distribution is unlimited.

Title:	Progress report on the incorporation of lower lengthscales into polycrystal plasticity models - Part 2
Author(s):	Subramanian, Gopinath Perez, Danny Uberuaga, Blas P. Tome, Carlos Voter, Arthur F.
Intended for:	Progress report Report



Disclaimer:

Los Alamos National Laboratory, an affirmative action/equal opportunity employer, is operated by the Los Alamos National Security, LLC for the National Nuclear Security Administration of the U.S. Department of Energy under contract DE-AC52-06NA25396. By approving this article, the publisher recognizes that the U.S. Government retains nonexclusive, royalty-free license to publish or reproduce the published form of this contribution, or to allow others to do so, for U.S. Government purposes. Los Alamos National Laboratory requests that the publisher identify this article as work performed under the auspices of the U.S. Department of Energy. Los Alamos National Laboratory strongly supports academic freedom and a researcher's right to publish; as an institution, however, the Laboratory does not endorse the viewpoint of a publication or guarantee its technical correctness.

Progress report on the incorporation of lower lengthscales into polycrystal plasticity models

Gopinath Subramanian Danny Perez Blas P. Uberuaga Carlos N. Tomé
Arthur F. Voter

UNCLASSIFIED: LA-UR # 12-00000

October 15, 2012

1 Introduction to Creep & Growth

Creep is the time-dependent, irreversible deformation that occurs at a low rate, at stresses below the ultimate stress of the material. Non-hydrostatic stresses (i.e. shear stresses) are required for creep. The kinds of creep relevant in cladding materials are (1) thermal creep, and (2) irradiation creep. These deformation processes require elevated temperatures, and applied stresses. Both processes are mediated by the motion of dislocations. Dislocations preferentially absorb either vacancies or interstitials, causing them to climb over obstacles. In thermal creep, the higher temperature causes high mobility of point defects, leading to a significant absorption rate of point defects by dislocations, leading to dislocation motion. In irradiation creep, the high radiation flux causes a supersaturation of point defects, that in turn leads to point defect absorption, and consequently dislocation motion.

Irradiation growth is defined as the irradiation induced dimensional changes that take place in the *absence* of applied stresses, and is caused by the partitioning of vacancies and interstitials among two or more kinds of sinks. Each kind of sink produces strain in a different crystallographic direction, such that the final deformation is anisotropic, and is volume conserved. In this phenomenon, the high radiation flux causes the supersaturation of point defects. These point defects then tend to aggregate into dislocation loops (either interstitial or vacancy). These loops then absorb more point defects, thereby growing in size, and leading to macroscopic strain.

The two phenomena of creep and growth become coupled in polycrystalline materials. Growth in a single grain is opposed by stresses caused by interaction of the growing grain with its neighbors (that are also growing, but in different directions). These stresses initiate and/or potentiate irradiation creep. In extreme cases, such as accident scenarios, thermal creep becomes important. Internal stresses in turn affect the diffusive characteristics of point defects within a grain, and consequently affecting the phenomenon of growth. In this report, we examine the coupling between creep and growth in a polycrystalline materials, and also look at the atomistic mechanisms that contribute to these phenomena.

2 Atomistics

The underlying fundamental mechanism that governs the creep and growth rates is the absorption of point defects (PDs) by sinks, such as dislocations, and dislocation loops. This fundamental

mechanism is considered to be the *unit process* of creep, and growth. The creep (and growth) rate, therefore, directly depends on the absorption rate of PDs by sinks. The individual character of sinks, however, causes them to absorb PDs at different rates. Upon absorbing defects, the sinks themselves evolve differently. The complex interplay between different absorption rates, distribution of sink populations due to cold work, nucleation of new sinks, and sink evolution ultimately contributes to the macroscopic creep and growth rate of the cladding.

We developed a framework that is capable of calculating absorption rates of PDs by sinks of arbitrary shape and size, and a population of these sinks. Calculations based on this framework can predict the constitutive law of single crystals, which can in turn inform mesoscale polycrystal plasticity models. We focus our attention on zirconium, the most widely used element in cladding material. PD types are restricted to single Self Interstitial Atoms (SIAs), and single vacancies (V), which renders the analysis presented here in the low neutron flux regime: PDs are far more likely to get absorbed by sinks, before they aggregate into defect clusters. Nevertheless, the framework presented here can be extended to handle SIA clusters and V clusters, and reactions between them. Here, we present an in-depth examination of (a) the polymorphism of single PDs, transitions between different polymorphs, and their importance; (b) the influence of strains on transitions, and consequently the mobility of PDs, and (c) the absorption rates of PDs by a variety of sinks, having arbitrary shapes and sizes using an object-KMC that takes into account both (a) and (b).

2.1 Methods

The need for examining the polymorphism of single PDs arises from some important observations of short-time molecular dynamics simulations of single SIAs in Zr. Firstly, a single SIA can exist in one of many polymorphs, or forms. SIAs of different polymorphs have different diffusion characteristics – e.g. a crowdion [1] is a one dimensional diffuser, aligned along a close packed direction. It has a high diffusivity along its alignment direction, but zero diffusivity along all others. Secondly, interconversion between polymorphs is seen frequently at most temperatures of interest. We have observed, as have others [2], that diffusion of SIAs in Zr is overall three dimensional. However, the 3D trajectory of a single SIA is punctuated by brief periods where it transforms into a crowdion, which then diffuses rapidly along a close packed direction, before transforming into one of the other polymorphs. These two observations show that the polymorphism, and rate of transition between polymorphs affect the overall diffusivity of a SIA, and consequently, the absorption rate of SIAs by sinks.

Another important effect that we account for is the strain-induced change in mobility of PDs. The local environment of a PD is affected by the strain field it experiences. The source of this strain field can either be external, or due to a nearby sink, such as a dislocation. The strain field perturbs the lattice atoms, and thereby changes the energy of the PD, and also the saddle point energies for transitions associated with the PD. The strain-induced change in the potential energy landscape can change the mobility of PDs in rather dramatic ways, and consequently, affects the absorption rate of PDs by sinks. The strain-induced change in energy can be accounted for by computing the dipole tensor \mathbf{G} , a quantity that is characteristic of an atomistic configuration (either PD, or saddle point). This allows us to account for the presence of an arbitrary strain field.

The first polymorph of a SIA was obtained by taking a perfect Zr lattice, placing a single additional atom in the octahedral position, and performing an energy minimization. This Octahedral polymorph (O) of a SIA was shown to be the ground state for a SIA by Willaime [3], and is consistent with our findings. For a vacancy (V), the first polymorph was obtained by removing an atom from the center of the simulation cell, and performing an energy minimization. All polymorphs were characterized using a scheme outlined by El-Mellouhi et al. [4], which we briefly describe. The

coordination number of all atoms was computed using a cutoff distance of 3.34\AA . All non-perfectly coordinated atoms, along with atoms within a sphere of radius 3.4\AA of the non-perfectly coordinated atoms were considered to be part of the defect. The atoms in this defect were numbered, and a connectivity graph based on the coordination analysis was generated, and stored in a database for future reference.

Figure 1 outlines the procedure used to discover transitions out of a given polymorph, and subsequently, all the different polymorphs. Starting from the minimized configuration of the polymorph, we ran high-temperature MD at 1100 K. Periodically, the “hot” point in the trajectory was quenched, and examined for the occurrence of a transition. A transition was declared to have occurred if the displacement of any atom between the original minimized configuration and the quenched hot point was greater than 0.6\AA . The displacement vector of the defect associated with this transition, \mathbf{dr} , was recorded. The polymorph at the end point of the transition was characterized using the coordination analysis described above, and a connectivity graph was generated for the end point. The connectivity graph of the end point was compared with all known connectivity graphs, using the automorphism detector NAutY [5], an open-source package [6]. NAutY examines two supplied connectivity graphs and reports if the two graphs have identical topology. We exploit this capability of NAutY to determine if two polymorphs are identical, barring rigid body transformations, including mirroring. If the end point of the transition was not recognized, it was classified as a new polymorph, and added to the database.

Each transition was characterized by computing the energy barrier using the nudged elastic band (NEB) method [7]. This method uses a chain of configurations connecting the initial and final states, with each configuration interacting with its neighbors on either side via a spring potential (the elastic band). The chain is “nudged” so that the components of the spring force are zero in directions perpendicular to the chain and components of the potential-induced gradient are zero in the direction tangential to the chain. The tangent at each point along the chain was computed using with the improved tangent estimation [8]. Upon convergence, the climbing image algorithm [9] was used to eliminate the sliding problem [7], and get the saddle point configuration.

We continued running high temperature MD until no new transitions out of the polymorph were discovered. We then repeated the procedure of running high temperature MD, transition characterization, and polymorph identification on all the newly discovered polymorphs. We iterated through this procedure until we were confident that we had discovered (a) all relevant polymorphs, and (b) all possible transitions for each polymorph. We are currently in the process of quantifying the confidence levels associated with this procedure..

As mentioned previously, the energetics of PDs, and transitions between polymorphs are affected by strain fields. The change in energy of a PD, or a saddle point associated with a transition, due to a strain ϵ is given by

$$\Delta E = -G_{ij}\epsilon_{ij} \quad (1)$$

where we have used the Einstein summation convention. It must be stressed that this value of ΔE is the change in energy of the defect alone, and does not contain the contribution due to elastic strain. Thus, in the procedure outlined below, the elastic contribution is always subtracted out. A variety of methods to compute the dipole tensor are available in the literature. In this study, we use Gillan’s strain derivative relation [10, 11], where we numerically extract the derivative of ΔE from equation 1 with respect to each of the strain components as follows:

In order to compute the ij^{th} component of the dipole tensor of a defect polymorph, we start with a relaxed structure of the polymorph. The simulation box is first subjected to a far-field, infinitesimal strain field component $\Delta\epsilon_{ij} > 0$, with all other strain components set to zero. The

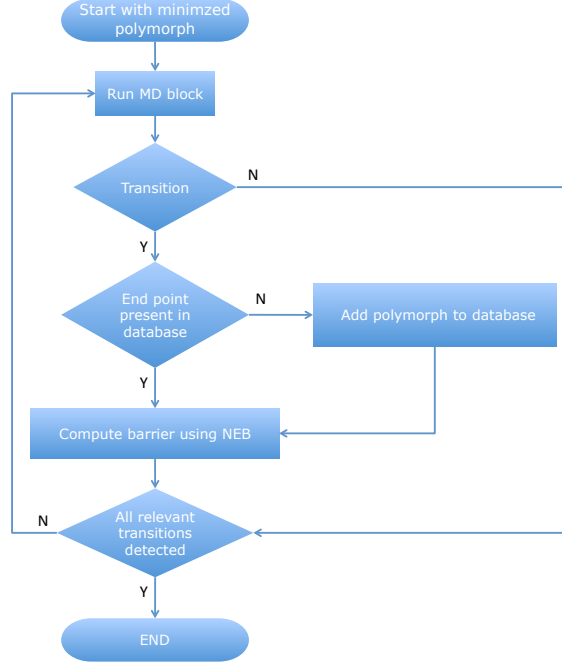


Figure 1: Flow chart illustrating the procedure used to discover polymorphs, and transitions between polymorphs.

boundary atoms are held fixed, while the rest of the structure is relaxed. The change in energy between the two relaxed structures is measured, and denoted as $\Delta(\Delta E)^+$.

In order to compute the ij^{th} component of the dipole tensor of the saddle point, the chain-of-states from the NEB calculation was taken to be the starting point. All images on the chain were subjected to an infinitesimal strain component $\Delta\epsilon_{ij} > 0$. The boundary atoms of all images on the chain were held fixed, and the NEB procedure was repeated to obtain a new saddle corresponding to the strained chain-of-states. The change in energy between the strained and unstrained saddles is measured, and denoted as $\Delta(\Delta E)^+$.

For both the polymorph, and saddle point, the energy change measurement is repeated with a strain $-\Delta\epsilon_{ij}$, and the change in energy obtained in this case is denoted as $\Delta(\Delta E)^-$. The value of G_{ij} , for both the polymorph and saddle point, is then given as

$$G_{ij} = -\frac{\Delta(\Delta E)^+ - \Delta(\Delta E)^-}{2\Delta\epsilon_{ij}} \quad (2)$$

The procedure is repeated for all components of the dipole tensor. We used $\Delta\epsilon_{ij} = 10^{-4}$ throughout. Note that this method of computing \mathbf{G} assumes that energy is linear with strain. It is conceivable that higher order terms might need to be included in equation 1, particularly in high strain situations.

2.2 Results

A single vacancy was observed to be capable of out-of-plane migration, and in-plane migration, with a barrier of 0.723 eV, and 0.637 eV, respectively. A single SIA, on the other hand, is more complex than a vacancy. It can exist in a variety of polymorphs, and shows a rich array of possible

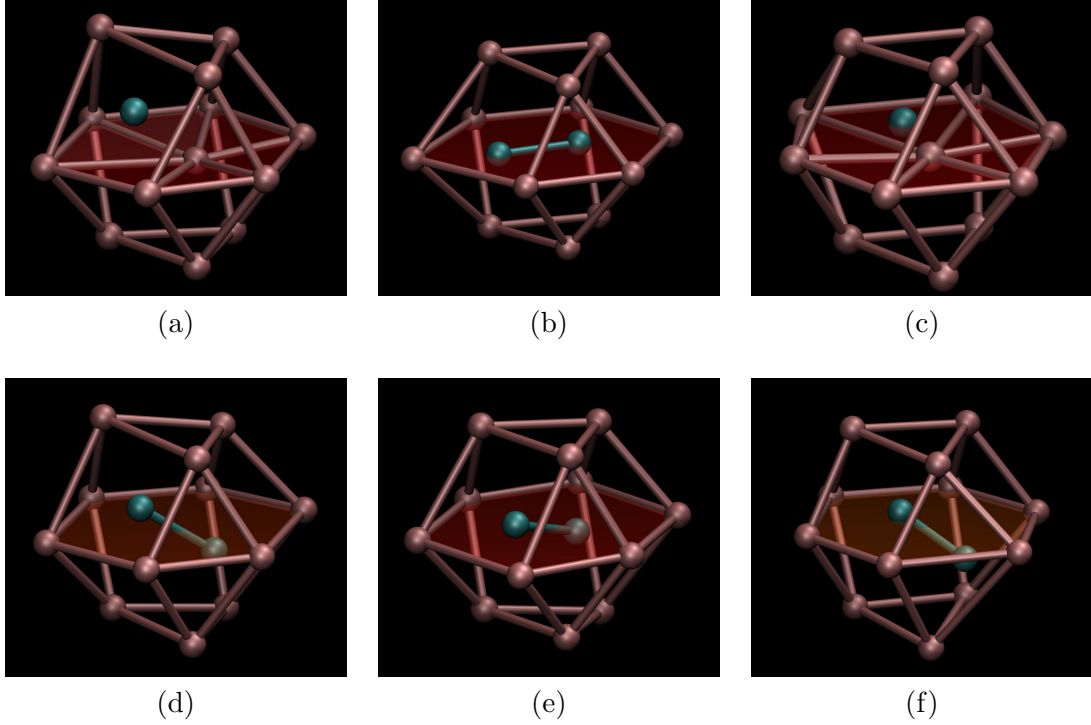


Figure 2: All possible polymorphs exhibited by a SIA. These configurations were carved out of fully relaxed minima. In all images, the $\langle 11\bar{2}0 \rangle$ direction is from the atom on the farthest left, to the atom on the farthest right. The basal plane is indicated in light red. The different polymorphs are (a) Octahedral (O), (b) Basal Crowdion, (c) Basal Octahedral, (d) – (f) Split types 1 – 3.

transformations between polymorphs. Figure 2 shows the six different types of polymorphs a SIA can exhibit. The ground state is the Octahedral (O) polymorph, shown in 2 (a). The other polymorphs are Basal Crowdion (BC), Basal Octahedral (BO), and three different types of Split (S-1, S-2, S-3). Three of the above polymorphs, viz. O, BO, and BC have been observed previously in DFT studies [3], while the three types of Split seem unique to the Mendelev-Ackland #3 potential. The polymorphism, possible transition, dipole tensor values, and displacements associated with each transition for single vacancies, and SIAs are shown in table 1.

The catalog of transitions for SIAs was used in an object-KMC simulation, and we describe some results from these simulations below. Similar simulations can be carried out for the vacancy. We first looked at the random walk trajectory of a SIA in an otherwise perfect crystal. The orientation of simulation axes with respect to crystal axes was chosen such that the X-axis was aligned along a close-packed direction, and the Z-axis was aligned along the c-direction, as shown in figure 3 (a). Figure 4 shows a plot of the mean square distance as a function of time, obtained as the average of 300 trajectories. Diffusion of a SIA is isotropic in the basal plane, and anisotropic overall. Increase in diffusivity due to an increase in temperature is seen, as expected.

We then ran a similar set of random walk trajectories, in the strained lattice, with $\varepsilon_{yy} = 0.005$. The effect of this strain is to introduce more free volume normal to the X-direction, and therefore, the diffusivity along the X-direction is increased by an order of magnitude. In other words, application of strain along the Y-direction breaks the symmetry of the basal plane, resulting in fully anisotropic diffusion.

We also investigated the behavior of a SIA in the vicinity of an edge dislocation. As the strain

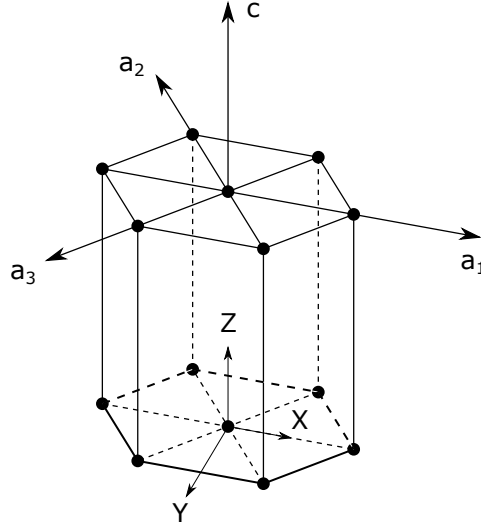


Figure 3: Orientation of single crystal with respect to the coordinate axes

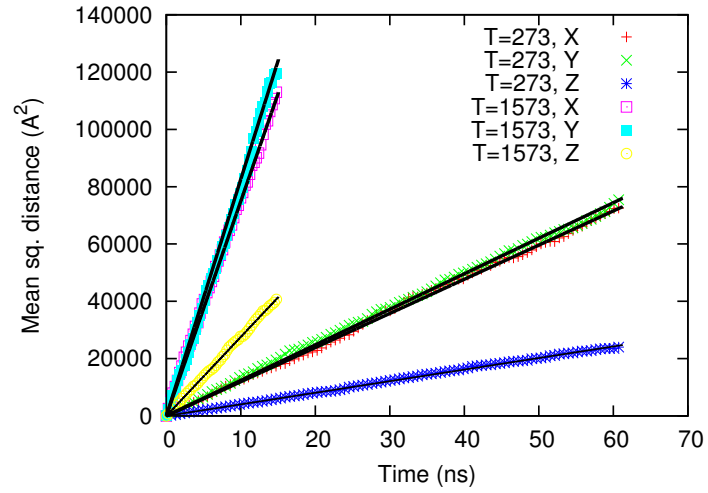


Figure 4: Mean square distance of a SIA at two different temperatures, in an otherwise perfect lattice. SIA diffusion is isotropic in the basal plane.

Table 1: List of dipole tensor values \mathbf{G} for all polymorphs, and transitions between polymorphs. Also given are the defect displacement values associated with each transition. This table does not include degeneracies due to crystal symmetry. Distances are in Å, while Energy and G_{ij} values are in eV. All SIA energies are relative to the ground state (Octahedral).

VACANCY										
polymorph	Energy				G_{11}	G_{22}	G_{33}	G_{23}	G_{13}	G_{12}
Vacancy (V)	0.0000				-4.70	-4.66	-5.23	-0.02	0.00	0.03
Transition	Saddle Energy	PD Displacement			G_{11}	G_{22}	G_{33}	G_{23}	G_{13}	G_{12}
		dx	dy	dz						
V \rightarrow V (Out-of-plane)	0.7227	0.00	1.87	2.58	-4.66	-6.74	-5.39	0.03	-0.01	2.83
V \rightarrow V (In-plane)	0.6369	3.23	0.00	0.00	-8.75	-2.81	-5.64	-0.05	0.00	0.48
SELF INTERSTITIAL ATOM (SIA)										
polymorph	Energy				G_{11}	G_{22}	G_{33}	G_{23}	G_{13}	G_{12}
Octahedral (O)	0.0000				10.53	10.15	12.66	0.27	-0.53	-0.22
Basal Crowdion (BC)	0.0925				11.96	9.53	7.26	-0.03	0.00	-0.02
Basal Octahedral (BO)	0.1173				9.77	9.68	5.05	-0.05	0.01	0.03
Split Type 1 (S-1)	0.0810				9.25	10.22	11.03	-0.03	-0.17	0.04
Split Type 2 (S-2)	0.1807				10.98	10.19	12.92	0.32	0.77	0.75
Split Type 3 (S-3)	0.1188				10.62	10.12	12.84	-0.18	-0.41	0.44
Transition	Saddle Energy	PD Displacement			G_{11}	G_{22}	G_{33}	G_{23}	G_{13}	G_{12}
		dx	dy	dz						
O \rightarrow O	0.0230	-1.70	0.00	0.00	11.27	10.60	12.95	0.14	-0.01	0.02
O \rightarrow S-1	0.0875	0.77	-0.05	-1.30	8.94	10.42	11.91	-0.21	0.05	-0.02
O \rightarrow S-2	0.1819	-0.60	-1.32	-0.95	11.26	10.87	-	-0.13	-0.57	-0.59
O \rightarrow S-3	0.1197	-0.85	-0.67	-1.57	11.32	10.59	13.02	0.15	-0.56	-0.60
S-1 \rightarrow BC	0.1269	-1.62	-0.31	0.00	12.40	9.69	8.14	1.50	2.89	1.55
S-2 \rightarrow BC	0.1812	0.71	-0.70	-0.35	11.22	10.90	13.21	-0.13	2.50	2.47
S-2 \rightarrow BO	0.1812	-0.25	-0.15	-0.35	11.66	9.41	9.41	1.35	0.02	0.01
S-3 \rightarrow BC	0.1209	0.00	0.31	-0.28	11.58	9.28	9.33	-1.35	0.00	0.06
BC \rightarrow BC	0.0954	3.23	0.00	0.00	11.80	9.60	7.26	-0.02	0.05	0.03
BC \rightarrow BO	0.1191	0.00	-1.11	0.00	10.11	9.37	5.19	-0.05	0.01	0.03

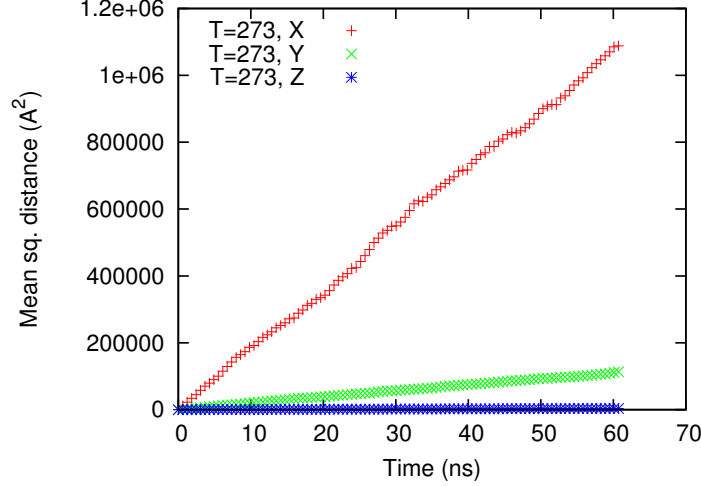


Figure 5: SIA diffusion in a strained lattice, with $\varepsilon_{yy} = 0.5$. This tensile strain breaks the symmetry of the basal plane, resulting in fully anisotropic diffusion.

field induced by the edge dislocation is needed as input to the object KMC, we looked to anisotropic elasticity to compute ε . For an edge dislocation in an HCP crystal with Burgers vector $\mathbf{b} = \mathbf{b}_x + \mathbf{b}_y$, the displacement field is given as [12]:

$$\begin{aligned}
 u_x &= -\frac{b_x}{4\pi} \left(\tan^{-1} \frac{2xy\lambda \sin \phi}{x^2 - \lambda^2 y^2} + \frac{\bar{c}_{11}'^2 - c_{12}'^2}{2\bar{c}_{11}'^2 c_{66}'} \sin 2\phi \ln \frac{q}{t} \right) \\
 &\quad - \frac{b_y}{4\pi \lambda \bar{c}_{11}'} \sin 2\phi \left[(\bar{c}_{11}' - c_{12}') \cos \phi \ln qt - (\bar{c}_{11}' + c_{12}') \sin \phi \tan^{-1} \frac{x^2 \sin 2\phi}{\lambda^2 y^2 - x^2 \cos 2\phi} \right] \\
 u_y &= \frac{\lambda b_x}{4\pi \bar{c}_{11}'} \sin 2\phi \left[(\bar{c}_{11}' - c_{12}') \cos \phi \ln qt - (\bar{c}_{11}' + c_{12}') \sin \phi \tan^{-1} \frac{y^2 \lambda^2 \sin 2\phi}{x^2 - \lambda^2 y^2 \cos 2\phi} \right] \\
 &\quad - \frac{b_y}{4\pi} \left(\tan^{-1} \frac{2xy\lambda \sin \phi}{x^2 - \lambda^2 y^2} + \frac{\bar{c}_{11}'^2 - c_{12}'^2}{2\bar{c}_{11}'^2 c_{66}'} \sin 2\phi \ln \frac{q}{t} \right)
 \end{aligned} \tag{3}$$

where

$$\begin{aligned}
 q^2 &= x^2 + 2xy\lambda \cos \phi + y^2 \lambda^2 \\
 t^2 &= x^2 - 2xy\lambda \cos \phi + y^2 \lambda^2 \\
 \bar{c}_{11}'^2 &= \sqrt{c_{11}' c_{22}'} \\
 \lambda &= \left(\frac{c_{11}'}{c_{22}'} \right)^4
 \end{aligned} \tag{4}$$

The strain field of the edge dislocation is then obtained by taking the derivatives of the dis-

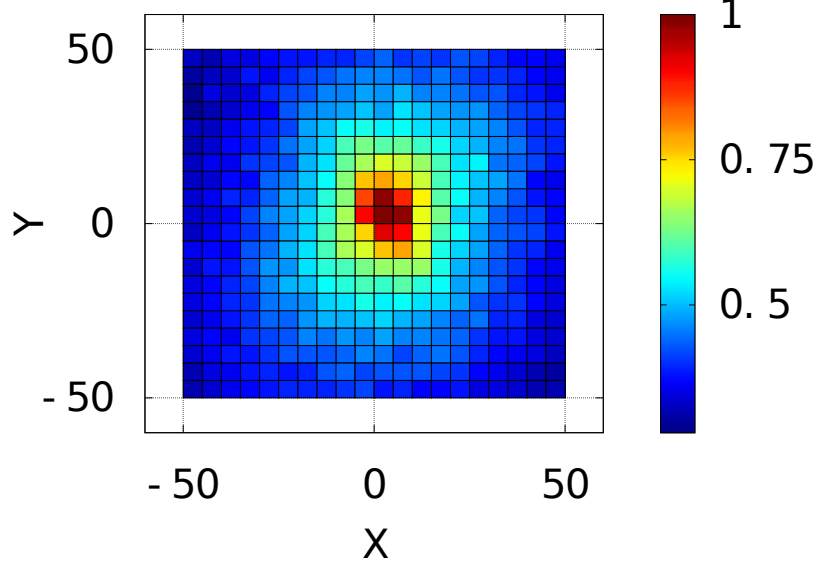


Figure 6: Capture probability of a SIA by an edge dislocation located at the origin with $\mathbf{b} = \frac{1}{3}\langle 11\bar{2}0 \rangle$, and line direction $\xi = z$. The anisotropy of the strain field is reflected in the anisotropy of the capture probability.

placement fields as:

$$\begin{aligned}
 \varepsilon_{xx} &= \frac{\partial u_x}{\partial x} \\
 \varepsilon_{yy} &= \frac{\partial u_y}{\partial y} \\
 \varepsilon_{xy} &= \frac{1}{2} \left(\frac{\partial u_x}{\partial y} + \frac{\partial u_y}{\partial x} \right) \\
 \varepsilon_{iz} &= 0 \quad \forall \quad i \in \{x, y, z\}
 \end{aligned} \tag{5}$$

Using this strain field, we then set up a simulation box with a single edge dislocation at the origin, with its line direction ξ aligned along the Z-axis. We then followed the path of a single SIA, starting at specific points in the simulation box, and counted the number of times a SIA was absorbed by the dislocation. The results of such a calculation, computed over 8.6×10^5 simulations are shown in figure 6.

3 Conclusions and Future directions

On the macroscale, we have demonstrated the coupling of polycrystal plasticity models with mesoscale growth models. The VPSC framework has been modified to include the growth model provided by ORNL, and the ability to swap it out for any other growth model that becomes available. On the atomistic side, we have demonstrated the capability to follow the dynamics of point defects in an arbitrary strain field.

We plan to extend the atomistic capability to handle point defect clusters. We also plan to compute similar quantities with Simon Philpott's new potential. We expect to collaborate more closely with ORNL to develop and improve upon their growth model, and feed it parameters computed from atomistics.

References

- [1] Heinz R. Paneth. The mechanism of self-diffusion in alkali metals. *Phys. Rev.*, 80:708–711, Nov 1950.
- [2] N. de Diego, A. Serra, D. J. Bacon, and Yu N. Osetsky. *Modelling and Simulation in Materials Science and Engineering*, 19(3):035003+, 2011.
- [3] F. Willaime. *Journal of Nuclear Materials*, 323:205, 2003.
- [4] Fedwa El-Mellouhi, Normand Mousseau, and Laurent J. Lewis. Kinetic activation-relaxation technique: An off-lattice self-learning kinetic monte carlo algorithm. *Phys. Rev. B*, 78:153202, Oct 2008.
- [5] B. D. McKay. Practical graph isomorphism. *Congressus Numerantium*, 30:45 – 87, 1981.
- [6] <http://cs.anu.edu.au/~bdm/nauty>.
- [7] H. Jónsson, G. Mills, and K. W. Jacobsen. Nudged elastic band method for finding minimum energy paths of transitions. In B. J. Berne, G. Ciccotti, and D. F. Coker, editors, *Classical and Quantum Dynamics in Condensed Phase Simulations*, page 385. World Scientific, 1998.
- [8] G. Henkelman and H. Jónsson. *Journal of Chemical Physics*, 113:9978, 2000.
- [9] Graeme Henkelman, Blas P. Uberuaga, and Hannes Jónsson. A climbing image nudged elastic band method for finding saddle points and minimum energy paths. *The Journal of Chemical Physics*, 113(22):9901–9904, 2000.
- [10] M. J. Gillan. The long-range distortion caused by point defects. *Philosophical Magazine A*, 48(6):903–919, 1983.
- [11] M J Gillan. The elastic dipole tensor for point defects in ionic crystals. *Journal of Physics C: Solid State Physics*, 17(9):1473, 1984.
- [12] J. P. Hirth and J. Lothe. Krieger Publishing Company, Malabar, Florida, 2 edition, 1992.